Nanoscale Research Letters

NANO EXPRESS Open Access

Synthesis of Cubic $Ni(OH)_2$ Nanocages Through Coordinating Etching and Precipitating Route for High-Performance Supercapacitors

Liangliang Tian[1*], Tong Yang[2], Wanrong Pu[3] and Jinkun Zhang[4]

Abstract

Rational design of cage-like structure is an effective method for the improvement of the capacitive performance of transition metal hydroxides. In this work, cubic Ni(OH)2 nanocages (Ni(OH)2 NCs) were constructed through a coordinating etching and precipitating (CEP) route. Ni(OH)2 NCs possess abundant active sites, sufficient diffusion channels, and accelerated electron transfer rate, which are beneficial for electrochemical kinetics. As a positive electrode for supercapacitors, the Ni(OH)2 NCs/Ni foam (NF) electrode presents a high specific capacitance of 539.8 F g^{-1} at 1 A g^{-1}, which is much larger than that of broken Ni(OH)2 NCs/NF (Ni(OH)2 BNCs/NF, 87.3 F g^{-1} at 1 A g^{-1}). In addition, the Ni(OH)2 NCs/NF electrode still retains 96.9% of its initial specific capacitance after 2000 cycles. The asymmetric supercapacitor (ASC) devices were assembled using Ni(OH)2 NCs/NF and activated carbon (AC)/NF as positive and negative electrodes, respectively. The ASC exhibits a higher energy density of 23.3 Wh kg^{-1} at a power density of 800 W kg^{-1} compared to Ni(OH)2 BNCs/NF (3 Wh kg^{-1} at 880 W kg^{-1}). These results demonstrate that the Ni(OH)2 NCs/NF electrode presents potential applications in the field of energy storage. The design of cage-like structure paves an effective way to achieve high-performance electrode materials.

Keywords: Transition metal hydroxides, $Ni(OH)_2$, Nanocages, Coordinating etching and precipitating, Supercapacitor, Energy storage

Background

To overcome the challenges of environment pollution and energy crisis, there are significant demands to develop safe, renewable, clean, and high-performance energy storage devices as alternatives to fossil fuels [1, 2]. Supercapacitors possess excellent characteristics to meet these issues, such as high-power capability (10–20 times that of batteries), high-rate performance, short charging time, and environment-friendly nature [3, 4]. Electric double-layer capacitors (EDLCs) and pseudocapacitors (PCs) are the commonly researched two types of supercapacitors. Thereinto, PCs governed by redox on/near the surface of transition metal oxide/hydroxide electrodes always have higher energy density than EDLCs and have become the hot issues in this field [5–10]. As a typical transition metal hydroxide, $Ni(OH)_2$ was reported as a high-performance electrode material for PCs due to the redox couple of Ni^{3+}/Ni^{2+} in an alkaline medium [11, 12]. Nevertheless, the acquired specific capacitance of $Ni(OH)_2$ is always much lower than the theoretical value because of the insufficient utilization of electrode materials.

Inspired by kinetics, the capacitive performance of electrode materials can be mediated through the design of microstructure and morphology. Tremendous efforts have been devoted to the synthesis of $Ni(OH)_2$ electrode materials with unique microstructures to achieve high-efficiency storage performance [13, 14]. Thereinto, constructing cage-like hollow porous structure was regarded as an effective method to obtain high-performance electrodes. Specifically, a cage-like structure can make full use of the inner and outer surface area and provide

* Correspondence: tyty216216@163.com
[1]Research Institute for New Materials Technology, Chongqing University of Arts and Sciences, Chongqing, People's Republic of China
Full list of author information is available at the end of the article

Springer Open

© The Author(s). 2019 **Open Access** This article is distributed under the terms of the Creative Commons Attribution 4.0 International License (http://creativecommons.org/licenses/by/4.0/), which permits unrestricted use, distribution, and reproduction in any medium, provided you give appropriate credit to the original author(s) and the source, provide a link to the Creative Commons license, and indicate if changes were made.

enough redox-active sites, leading to enhanced specific capacitance. Furthermore, the porous shell affords amounts of diffusion paths for electrolyte, which is beneficial to the reversibility of the electrode, resulting in excellent cycling stability and high-rate performance. Regarding electron transfer kinetics, the nanosized thin shell refines the transfer route of electrons and accelerates the electron transfer rate [15, 16]. Thus, higher capacitive performance of $Ni(OH)_2$ can be obtained through the design of cage-like hollow porous architecture.

The templated chemical process is the commonly used method to prepare cage-like architectures [17, 18]. The final products can accurately duplicate the geometrical shape of the templates and retain a well-defined morphology with narrow size distribution [19, 20]. In this work, $Ni(OH)_2$ NCs were fabricated using cubic Cu_2O crystals as sacrificial templates through thiosulfate involved coordinating etching and precipitating (CEP) principle. The synthesized $Ni(OH)_2$ NCs/NF was employed as positive electrode for supercapacitors and $Ni(OH)_2$ BNCs/NF was introduced as a contrast sample to confirm the structural advantages of cage-like architecture. $Ni(OH)_2$ NCs/NF displays a high specific capacitance of 539.8 F g^{-1} at 1 A g^{-1}, which is much larger than that of $Ni(OH)_2$ BNCs/NF (87.3 F g^{-1} at 1 A g^{-1}). The asymmetric supercapacitor (ASC) device presents a high energy density of 23.3 Wh kg^{-1} at 800 W kg^{-1}, and this value is much larger than that of $Ni(OH)_2$ BNCs/NF//AC (3 Wh kg^{-1} at 880 W kg^{-1}). The results reveal that $Ni(OH)_2$ NCs/NF electrode exhibits an attractive prospect in supercapacitors. The way to design cage-like hollow porous architecture is also meaningful in other fields, such as sensors and catalysts.

Methods/Experimental

Preparation of Cu_2O Templates

Cubic Cu_2O crystals were synthesized according to our previous report [21]. Fifty milliliters NaOH solution (2 M) was added into the stirred $CuCl_2{\cdot}2H_2O$ (500 ml, 0.01 M) within 3 min at 55 °C. After stirring for 30 min, 50 mL 0.6 M ascorbic acid solution was added dropwise. The final samples were centrifugated after 3 h and dried in a vacuum.

Synthesis of $Ni(OH)_2$ NCs

400 mg Cu_2O templates and different dosage of $NiCl_2$ powers were poured into a 1000-mL beaker containing 400 mL mixed water and alcohol (volume ratio = 1:1). The mass ratio of Cu_2O templates and $NiCl_2$ powers is controlled as 5:1, 2.5:1, 1.67:1, and 1.25:1 (corresponding $NiCl_2$ dosage is 80 mg, 160 mg, 240 mg, and 320 mg, respectively). After ultrasonic treatment for 10 min, 13.2 mg polyvinyl pyrrolidone (PVP) was dispersed into the solution under stirring. After 30 min, 160 mL 1 M $Na_2S_2O_3$ was added dropwise into the solution at room temperature. After 3 h, the final products were collected by centrifugation and dried in an oven. $Ni(OH)_2$ BNCs were obtained through the ultrasonic treatment of $Ni(OH)_2$ NCs for 2 h in alcohol (Additional file 1: Figure S1).

Materials Characterizations

The structure and chemical composition of the products were analyzed by X-ray powder diffraction (XRD, Rigaku D/Max-2400) using Cu Kα radiation and ESCALAB 250Xi X-ray photoelectron spectroscopy (XPS, USA). The morphologies of the products were investigated on a Zeiss Gemini 300 field emission scanning electron microscopy (FESEM). Transmission electron microscope (TEM) observations were conducted on a FEI F20 device. The specific surface area and porous feature were measured on a Belsort-max instrument.

Electrochemical Measurements

All the electrochemical measurements were performed on a μIII Autolab workstation in 3 M KOH with Pt foil (1 cm × 1 cm) and Ag/AgCl (saturated KCl) as counter and reference electrodes, respectively. The working electrodes were constructed by the following procedures: first, the electrode materials ($Ni(OH)_2$ NCs obtained at different reaction time and $Ni(OH)_2$ BNCs), acetylene black, and polytetrafluoro ethylene (5% PTFE) were mixed together with a mass ratio of 80:15:5 in ethanol. And then, the mixture was coated onto NF (1 cm × 1 cm) and dried in an oven. The loading mass was calculated as 3.4 mg/cm^2. The electrochemical performance was examined by cyclic voltammetry (CV), galvanostatic charge-discharge (GCD), and electrochemical impedance (EIS). The EIS tests were performed between 0.01 and 100 kHz with a perturbation amplitude of 5 mV. The specific capacitance of the electrodes was calculated according to the following equation:

$$C = \frac{I\Delta t}{m\Delta V} \tag{1}$$

where I is the discharge current (A), t is the discharge time (s), ΔV is the potential window (V), m is the total mass (g) of electrode materials. The ASCs were prepared with $Ni(OH)_2$ NCs (or $Ni(OH)_2$ BNCs)) and AC as the positive and negative electrodes, respectively. The AC electrode was prepared by coating a mixture of AC and PTFE binder (90:10) on NF (1 cm × 1 cm). Then the two electrodes were assembled together with a separator in 3 M KOH.

Results and Discussions

Characterizations

XRD pattern of the prepared $Ni(OH)_2$ NCs was recorded in Fig. 1a. The observed three strong peaks located at 33.1°, 38.5°, and 60.2° correspond to (100), (101), and (003) crystalline planes of hexagonal β-$Ni(OH)_2$ (JCPDS no. 14-0117) [22]. XPS measurements were conducted to confirm the chemical composition. Ni, O, and C signals are clearly observed in the survey spectrum, revealing that the sample is mainly composed of Ni and O. As displayed in Fig. 1c, the concentrated signals located at 873.7 eV and 856.1 eV with a separation of 17.6 eV can be attributed to Ni $2p_{1/2}$ and Ni $2p_{3/2}$ of Ni^{2+}, respectively [23, 24]. The peaks located at 879.9 eV and 861.7 eV are the corresponding satellite signals for Ni $2p_{1/2}$ and Ni $2p_{3/2}$, respectively. As shown in Fig. 1d, the O1s peak located at 531.2 eV presents a typical feature of Ni-O-Ni bond in $Ni(OH)_2$ [25, 26]. On the basis of the above discussions, the as prepared products can be deduced to $Ni(OH)_2$ phase.

SEM and TEM observations were employed to further confirm the morphology feature of the products. Additional file 1: Figure S2a displays the XRD pattern of the prepared Cu_2O. All the diffraction peaks can be indexed to JCPDS no. 78-2076, confirming the successful preparation of Cu_2O. SEM image of Cu_2O templates in Additional file 1: Figure S2b reveals cubic feature of the products with an edge length about 500 nm. As noticed in Fig. 2a, the $Ni(OH)_2$ samples retain uniform well-defined cubic morphology after the CEP process. The $Ni(OH)_2$ cubes have an edge length of 500 nm (Fig. 2b), which is more or less the same as Cu_2O templates. As can be seen from the inset of Fig. 2b, the surface of $Ni(OH)_2$ cubes is composed of quantities of fine particles and presents porous characteristic. The TEM image in Fig. 2c exhibits apparent internal cavity, revealing the cage-like feature of $Ni(OH)_2$ products. As displayed in Fig. 2d, the edge length is of 500 nm, which is consistent with the observation of SEM. Moreover, the shell thickness of $Ni(OH)_2$ NCs is identified as 50 nm (Fig. 2d). The investigations of SEM and TEM demonstrate the cage-like feature of the products. The cage-like hollow porous structure provides a large surface area and amounts of diffusion paths, which may favor the mass transport process, leading to outstanding capacitive performance.

The optical photographs and TEM images of $Ni(OH)_2$ NCs were recorded at different reaction times to realize the formation mechanism. As displayed in Fig. 3a, the reaction solution exhibits brick-red color at 5 min, indicating that little reactions occur at the initial stage. Afterwards, the color of the solution gradually becomes lighter. After 3 h, the color of the solution turns into light green, which is the color of the final products. As illustrated in Fig. 3b, the products present partly hollow internal cavity due to the dissolution of Cu_2O templates at 5 min. Moreover, the etching of internal Cu_2O preferentially occurred at the corner owing to the adequate diffusion kinetics. The internal Cu_2O crystals dissolve continuously until it completely disappears at 3 h. The schematic diagram was illustrated in Scheme 1.

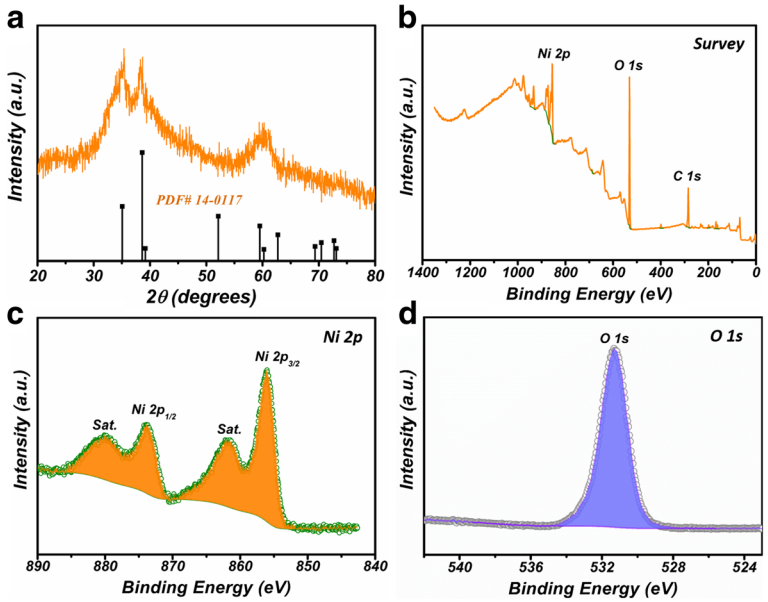

Fig. 1 **a** XRD pattern of the prepared $Ni(OH)_2$ NCs. **b**–**d** XPS spectra of the $Ni(OH)_2$ NCs. **b** Survey. **c** Ni 2p. **d** O 1s

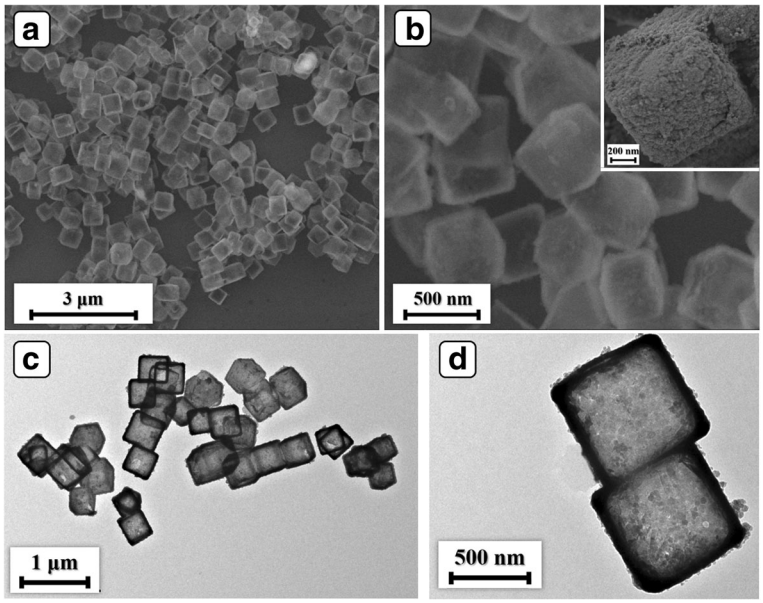

Fig. 2 **a**, **b** SEM and **c**, **d** TEM images of the $Ni(OH)_2$ NCs

Generally, the formation mechanism of $Ni(OH)_2$ NCs is shown below (Eq. (2)):

$$Ni^{2+} + 2OH^- \rightarrow Ni(OH)_2 \quad (2)$$

Ni^{2+} ions in Eq. (2) are the absorbed Ni^{2+} on the surface of Cu_2O crystals (Step 1). OH^- ions in Eq. (2) are released from the corrosion of Cu_2O crystals (Eq. (3)) and hydrolyzation of $S_2O_3^{2-}$ (Eq. (4)).

$$Cu_2O + xS_2O_3^{2-} + H_2O \rightarrow \left[Cu_2(S_2O_3)_x\right]^{2-2x} + 2OH^- \quad (3)$$

$$S_2O_3^{2-} + H_2O \rightarrow HS_2O_3^{2-} + OH^- \quad (4)$$

Equations (3) and (4) are the mechanism for $S_2O_3^{2-}$ involved CEP process, which happens in Steps 2 and 3. The detailed kinetics process is similar to the formation of $Co(OH)_2$ NCs in our published article [27]. The transport of $S_2O_3^{2-}$ towards Cu_2O determines the corrosion rate and the released OH^- ions from interior

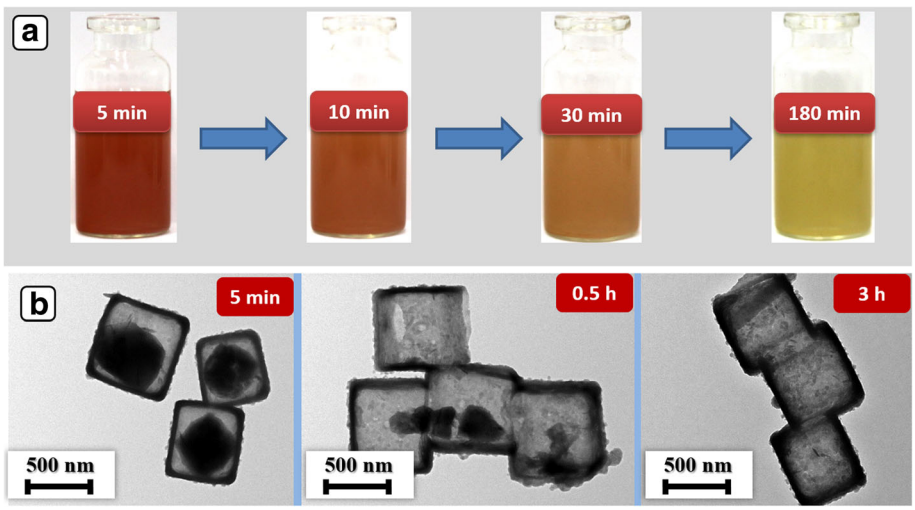

Fig. 3 **a** The optical photographs of the reaction system at a different reaction time. **b** TEM images of the products obtained at different reaction time

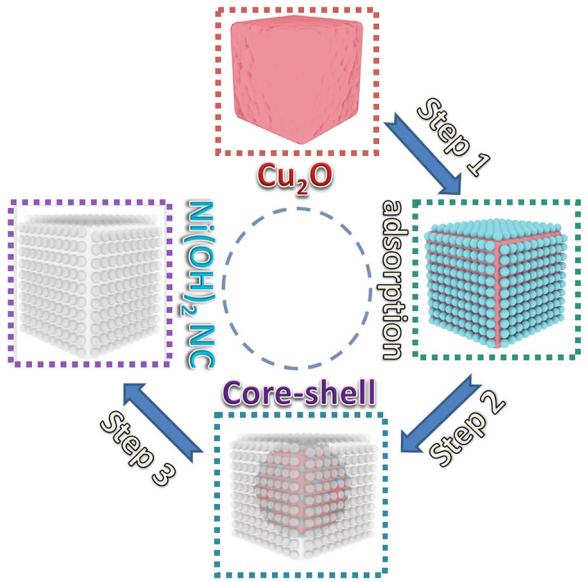

Scheme 1 Schematic diagram for the formation process

presents the growth rate of $Ni(OH)_2$ NCs. The cooperative control of the two processes results in the formation of well-defined $Ni(OH)_2$ NCs.

Fig. 4 shows the N_2 adsorption-desorption isotherm curves of $Ni(OH)_2$ NCs and $Ni(OH)_2$ BNCs. The BET surface area of $Ni(OH)_2$ NCs is 54.7 m^2/g, which is much larger than that of $Ni(OH)_2$ BNCs (38.1 m^2/g). The results indicate that the hollow porous architecture endows $Ni(OH)_2$ NCs with a larger specific surface area. The pore size distributions (insets of a and b) reveal the mesoporous structure of $Ni(OH)_2$ NCs and $Ni(OH)_2$ BNCs. The pore volume of $Ni(OH)_2$ NCs is calculated as 0.25 cm^3/g, which is larger than $Ni(OH)_2$ BNCs (0.19 cm^3/g). Furthermore, a concentrated pore distribution between 2.7 and 6.1 nm is investigated for $Ni(OH)_2$ NCs, which is related to the interspace between nanoparticles. However, no obvious concentrated pore distribution is observed for $Ni(OH)_2$ BNCs, revealing the destruction of ordered diffusion channels. The large surface area and ordered diffusion channels are beneficial for electrochemical kinetics, resulting in excellent capacitive performance.

Electrochemical Performance of $Ni(OH)_2$ NCs

In order to obtain the best capacitive property, $Ni(OH)_2$ NCs with different shell thickness were prepared by controlling the dosage of $NiCl_2$ powders. As shown in Fig. 5, the shell thickness apparently increases from 27.4 to 76.7 nm with the increase of mass ratio from 5:1 to 1.67:1. However, the shell thickness only slightly increases from 76.7 nm to 79 nm with the further increase of mass ratio to 1.25:1. The results can be attributed to the kinetics difficulty in mass diffusion caused by the hindering of shell. The GCD curves of $Ni(OH)_2$ NCs obtained with different $NiCl_2$ dosage were measured and the data were recorded in Fig. 6a. It is clear that the sample with $Cu_2O/NiCl_2$ 2.5:1 displays the longest discharge time under 4 A/g, indicating the best capacitive performance. This result can be ascribed to the suitable mass transport kinetics derived from the moderate shell thickness. Furthermore, the capacitive performance of $Ni(OH)_2$ NCs obtained with $Cu_2O/NiCl_2$ 2.5:1 was contrastively evaluated with $Ni(OH)_2$ BNCs. As shown in Fig. 6b, significant redox peaks are clearly observed in the CV curves of $Ni(OH)_2$ NCs and $Ni(OH)_2$ BNCs, revealing pseudocapacitive characteristic of the two electrodes. The redox process corresponds to the storage mechanism related to $Ni(OH)_2/NiOOH$ redox couple illustrated in Eq. (5) [28, 29].

$$Ni(OH)_2 + OH^- \leftrightarrow NiOOH + H_2O + e^- \quad (5)$$

The CV encapsulated area of $Ni(OH)_2$ NCs is much larger than that of $Ni(OH)_2$ BNCs, demonstrating higher

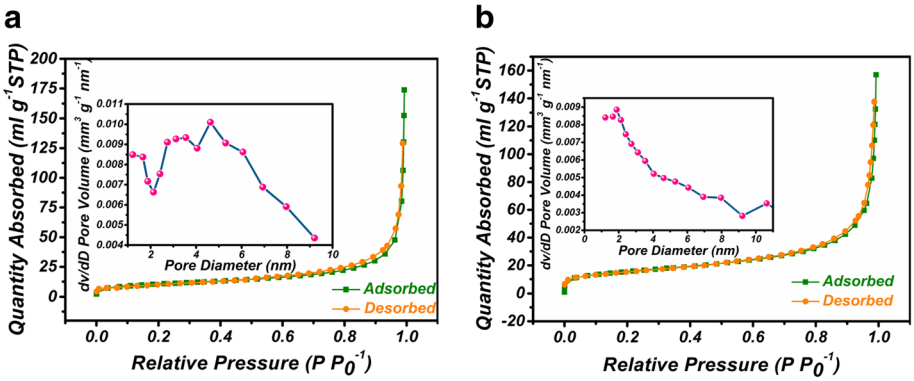

Fig. 4 BET measurements of **a** $Ni(OH)_2$ NCs and (b) $Ni(OH)_2$ BNCs. Insets of **a** and **b** are the corresponding pore size distributions of $Ni(OH)_2$ NCs and $Ni(OH)_2$ BNCs, respectively

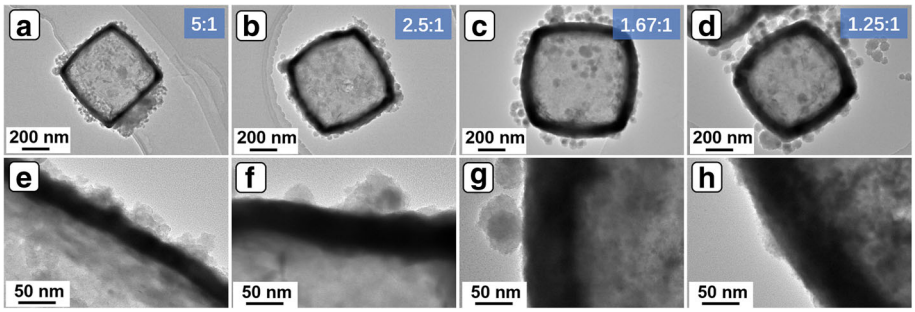

Fig. 5 **a**–**d** TEM images of the $Ni(OH)_2$ NCs obtained with different mass ratio of $Cu_2O/NiCl_2$. **e**–**h** TEM images of the corresponding shells of **a**–**d**

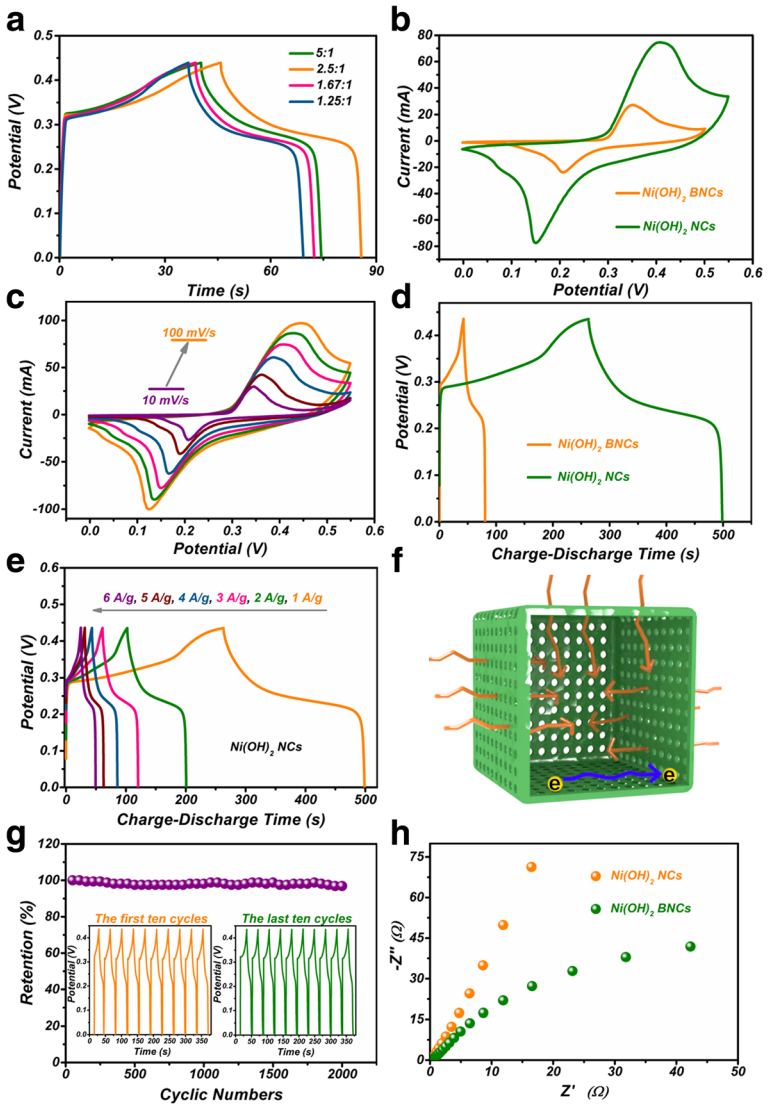

Fig. 6 **a** GCD curves of the products obtained with different mass ration of $Cu_2O/NiCl_2$ at 4 A g^{-1}. **b** The CVs of $Ni(OH)_2$ NCs/NF and $Ni(OH)_2$ BNCs/NF at scan rate of 60 mV/s. **c** The CVs of $Ni(OH)_2$ NCs/NF at different scan rates. **d** GCD curves of $Ni(OH)_2$ NCs/NF and $Ni(OH)_2$ BNCs/NF at 1 A g^{-1}. **e** GCD curves of $Ni(OH)_2$ NCs/NF at different current densities. **f** The schematic of charge storage advantages for $Ni(OH)_2$ NCs. **g** The cycling stability of $Ni(OH)_2$ NCs/NF at 8 A g^{-1}. **h** The EIS spectra of $Ni(OH)_2$ NCs/NF and $Ni(OH)_2$ BNCs/NF

specific capacitance. The CVs of $Ni(OH)_2$ NCs at various scan rates are depicted in Fig. 6c. The CV curve still retains a well-defined shape even at a high scan rate of 100 mV/s, demonstrating outstanding rate capability and high electrochemical reversibility. Furthermore, the peak current linearly increases with the square root of scan rates, revealing that bulk diffusion is the dominated factor (Additional file 1: Figure S3). As presented in Fig. 6d, the GCD curves of $Ni(OH)_2$ NCs show longer discharge time than $Ni(OH)_2$ BNCs at 1 A g^{-1}, proving that $Ni(OH)_2$ NCs exhibit higher specific capacitance than $Ni(OH)_2$ BNCs. Fig. 6e presents the GCD curves of $Ni(OH)_2$ NCs at different current densities. The calculated specific capacitances for $Ni(OH)_2$ NCs are 539.8, 445.5, 409.4, 391.3, 360.2, and 340.7 F g^{-1} at 1, 2, 3, 4, 5, and 6 A g^{-1}, respectively (Additional file 1: Figure S4). Those values calculated for $Ni(OH)_2$ BNCs are 87.3, 77.4, 72.9, 67.8, 64.1, and 60.5 F g^{-1} at corresponding current density (Additional file 1: Figure S5). The structural advantages for $Ni(OH)_2$ NCs are illustrated in Fig. 5f. First, the cage-like feature provides quantities of active sites for Faraday reactions. Secondly, the porous thin shell shortens the migration distance of electrons, resulting in high electron transfer rate. Third, the porous shell affords sufficient diffusion channels for electrolyte, improving the utilization rate of $Ni(OH)_2$. The cycling stability of $Ni(OH)_2$ NCs was evaluated by repeating the GCD measurements at 8 A g^{-1} (Fig. 6 g). It is noticed that the specific capacitance still retains 96.9% of its initial value after 2000 cycles, which is much larger than that of $Ni(OH)_2$ BNCs (61.5%, Additional file 1: Figure S6). As shown in the inset, the last 10 cycles show little difference compared to the first 10 charge-discharge cycles, revealing excellent stability. The little attenuation of the capacitance can be attributed to the small amount of shedding of $Ni(OH)_2$ NCs from NF. The internal void and pores in the shell afford enough space for the release of a strain during the cycling process [30].

In order to confirm the advantages of cage-like structure in kinetics, EIS spectra were recorded in Fig. 6h and the equivalent circuit was illustrated in Additional file 1: Figure S7. The equivalent circuit is mainly composed of Rs, Rct, Zw, CPE, and CL. Thereinto, Rs is internal resistance of the electrode system. Rct is the charge transfer resistance related to the radius of semicircle in EIS spectra. Zw is the Warburg impendence corresponding to the slope of EIS in high frequency. Although $Ni(OH)_2$ NCs/NF electrode has more or less the same Rs value (0.27 Ω) compared to $Ni(OH)_2$ BNCs/NF (0.25 Ω), $Ni(OH)_2$ NCs/NF has a much lower Rct (120.8 Ω) than that of $Ni(OH)_2$ BNCs (976.5 Ω), revealing higher electron transfer rate. The high electron transfer rate can be attributed to enough thin shell of $Ni(OH)_2$ NCs. Apparently, $Ni(OH)_2$ NCs/NF electrode presents a much larger slope than $Ni(OH)_2$ BNCs/NF, demonstrating more straightway diffusion process. The unimpeded diffusion can be ascribed to the ordered channels and porous characteristic of $Ni(OH)_2$ NCs/NF electrode. On the basis of the above discussions, $Ni(OH)_2$ NCs/NF electrode possesses significant advantages in electrochemical kinetics compared to $Ni(OH)_2$ BNCs/NF.

Electrochemical Performance of the ASC device

The ASC device of $Ni(OH)_2$ NCs/NF//AC was constructed according to Fig. 7a. $Ni(OH)_2$ NCs/NF electrode and AC were separated by a cellulose paper. As illustrated in Fig. 7b, the CV curve of AC electrode presents nearly rectangular feature, revealing typical EDLC storage mechanism. Moreover, the AC electrode can be cycled within − 1 to 0 V and $Ni(OH)_2$ NCs/NF electrode can be cycled within 0 to 0.6 V, revealing that the ASC device can afford an operation voltage of 1.6 V. The CV curves displayed in Fig. 7c show a well-defined shape even at high scan rates, implying excellent mass transport kinetics and eminent reversibility. GCD curves of the ASC device at different current densities were shown in Fig. 7d. The energy density and power density of the device were calculated according to Fig. 7d. An energy density of 23.3 Wh Kg^{-1} is achieved at a power density of 800 W Kg^{-1}. An energy density of 9.6 Wh Kg^{-1} is still obtained even at a high power density of 8000 W Kg^{-1}. The energy density is much larger than that of $Ni(OH)_2$ BNCs/NF//AC ASC (Additional file 1: Figure S8, 3 Wh Kg^{-1} at 880 W Kg^{-1}). Furthermore, the maximum energy density of the ASC is also larger than those of $Ni(OH)_2$-based materials [31, 32]. The cycling stability was estimated by repeating GCD measurements at 4 A g^{-1} for 2000 cycles. The final specific capacitance still retains 90.1% of its largest value and this value is much larger than that of $Ni(OH)_2$ BNCs/NF//AC ASC (Additional file 1: Figure S9, 60%). In addition, the last ten GCD curves are similar to the first ten cycles, exhibiting excellent stability of the ASC device. As shown in Fig. 7f, $Ni(OH)_2$ NCs still retain the uniform cubic cage-like morphology after 2000 cycles, further demonstrating the excellent cycling stability. The loss of the specific capacitance may be attributed to the small amount of active material dropping from NF.

Conclusions

Overall, $Ni(OH)_2$ NCs were successfully constructed through a CEP method and used as an electrode for supercapacitors. $Ni(OH)_2$ NCs present a large specific surface area of 54.7 m^2/g and a concentrated pore size distribution between 2.7 and 6.1 nm. The thin shell shortens the transfer route and improves the electron transfer rate. As a positive electrode for supercapacitors, $Ni(OH)_2$ NCs/NF displays a specific capacitance of 539.8 F g^{-1} at 1 A g^{-1}, which is much larger than that of

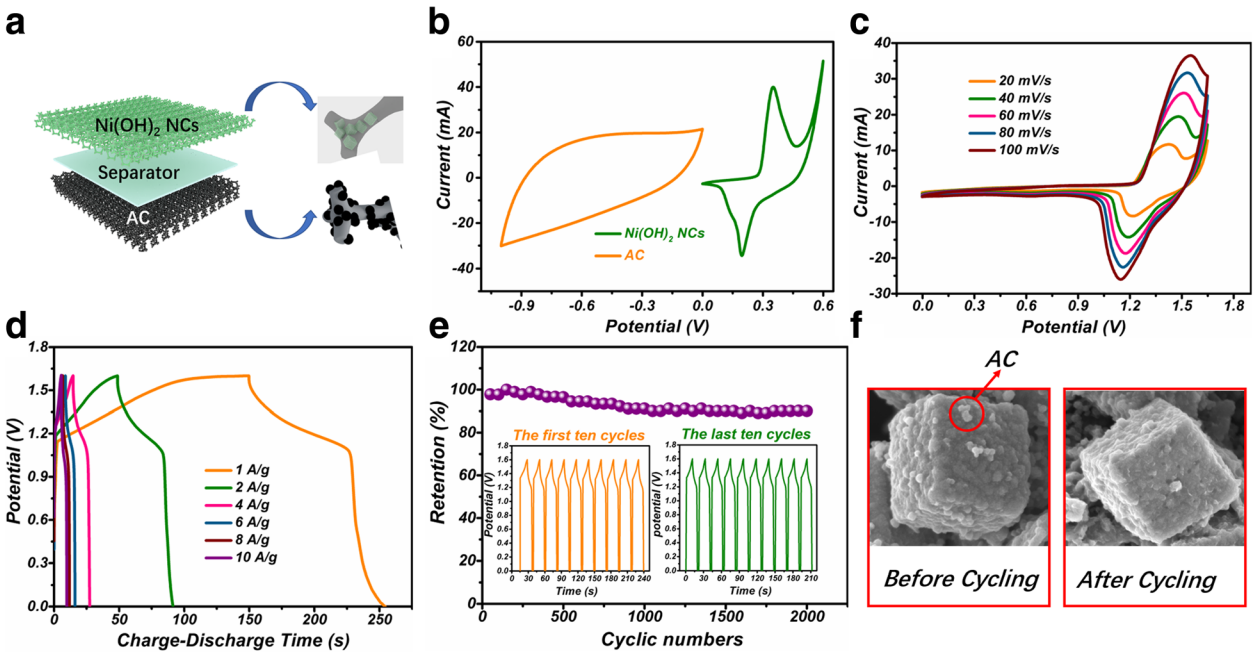

Fig. 7 **a** Schematic of the $Ni(OH)_2$ NCs/NF//AC device. **b** The CVs of AC and $Ni(OH)_2$ NCs/NF electrodes in a three-electrode system. **c** The CVs of $Ni(OH)_2$ NCs/NF//AC ASC between 0 and 1.6 V. **d** GCD curves of the ASC at different current densities between 0 and 1.6 V. **e** Cycling stability of the ASC during 2000 cycles at 4 A g^{-1}. **f** The SEM images of the positive electrode before and after the cycling

$Ni(OH)_2$ BNCs/NF//AC (87.3 F g^{-1} at 1 A g^{-1}). The specific capacitance still retains about 96.9% of its initial value after 2000 cycles. The ASC of $Ni(OH)_2$ NCs/NF//AC possesses an energy density of 23.3 Wh Kg^{-1} at 800 W Kg^{-1}, which is much larger than that of $Ni(OH)_2$ BNCs (3 Wh Kg^{-1} at 880 W Kg^{-1}). The results demonstrate that the designed $Ni(OH)_2$ NCs have potential applications in the field of energy storage.

Additional Files

Additional file 1: Figure S1. SEM image of the $Ni(OH)_2$ BNCs sample. **Figure S2.** (a) XRD pattern and (b) SEM image of Cu_2O templates. **Figure S3.** The relationship between peak current and square root of scan rates. **Figure S4.** The relationship between specific capacitance and charging-discharging current densities for $Ni(OH)_2$ NCs/NF. **Figure S5.** (a) The GCD curves of $Ni(OH)_2$ BNCs/NF at different current densities; (b) The relationship between specific capacitance and current densities for $Ni(OH)_2$ BNCs/NF. **Figure S6.** The cycling stability of $Ni(OH)_2$ BNCs/NF. **Figure S7.** The equivalent circuit of EIS. **Figure S8.** The GCD curves of $Ni(OH)_2$ BNCs/NF//AC at different current densities. **Figure S9.** The cycling stability of $Ni(OH)_2$ BNCs/NF//AC. (DOC 2752 kb)

Abbreviations

AC: Activated carbon; ASC: Asymmetric supercapacitor; BNCs: Broken nanocages; CEP: Coordinating etching and precipitating; CV: Cyclic voltammetry; EDLCs: Electric double-layer capacitors; EIS: Electrochemical impedance spectroscopy;; FESEM: Field emission scanning electron microscope; GCD: Galvanostatic charge-discharge; NCs: Nanocages; NF: Ni foam; PCs: Pseudocapacitors; PTFE: Polytetrafluoro ethylene; PVP: Polyvinyl pyrrolidone; TEM: Transmission electron microscope; XPS: X-ray photoelectron spectrometer; XRD: X-ray diffraction

Acknowledgements

We greatly appreciate the funding of the National Natural Science Foundation of China (21403020), Basic and Frontier Research Program of Chongqing Municipality (cstc2016jcyjAX0014, cstc2016jcyjAX0148), Scientific and Technological Research Program of Chongqing Municipal Education Commission (KJ1601133, KJ1711269, KJ1711267), and Foundation of Chong Qing University of Arts and Science (P2018cl07, M2017ME19, M2018ME04).

Authors' Contributions

LLT designed the experiment and wrote the paper. TY did the electrochemical measurements. WRP prepared the materials and JKZ made the characterizations. All authors read and approved the final manuscript.

Funding

This study was financially supported by the funding of the National Natural Science Foundation of China (21403020), Basic and Frontier Research Program of Chongqing Municipality (cstc2016jcyjAX0014, cstc2016jcyjA0148), Scientific and Technological Research Program of Chongqing Municipal Education Commission (KJ1601133, KJ1711269, KJ1711267), and Foundation of Chong Qing University of Arts and Science (P2018cl07, M2017ME19, M2018ME04).

Availability of Data and Materials

The datasets are available without restriction.

Competing Interests

The authors declare that they have no competing interests.

Author details

[1]Research Institute for New Materials Technology, Chongqing University of Arts and Sciences, Chongqing, People's Republic of China. [2]Faculty of Materials and Energy, Southwest University, Chongqing, People's Republic of China. [3]School of Pharmacy, Tianjin Medical University, Tianjin, People's Republic of China. [4]College of Pharmaceutical Science, Zhejiang University of Technology, Zhejiang, People's Republic of China.

Received: 14 April 2019 Accepted: 21 July 2019
Published online: 02 August 2019

References

1. Jiang J, Li YY, Liu JP, Huang XT, Yuan CZ, Lou XL (2012) Recent advances in metal oxide-based electrode architecture design for electrochemical energy storage. Adv Mater 24:5166–5180
2. Hu LY, Dai CL, Liu H, Li Y, Shen BL, Chen YM, Bao SJ, Xu MW (2018) Double-shelled NiO-$NiCo_2O_4$ heterostructure@carbon hollow nanocages as an efficient sulfur host for advanced lithium–sulfur batteries. Adv Energy Mater 8:1800e709
3. Simon P, Gogotsi Y (2008) Materials for electrochemical capacitors. Nat Mater 7:845–854
4. Yan J, Wang Q, Wei T, Fan ZJ (2014) Recent advances in design and fabrication of electrochemical supercapacitors with high energy densities. Adv Energy Mater 4:1300816
5. Lang XY, Hirata A, Fujita T, Chen MW (2011) Nanoporous metal/oxide hybrid electrodes for electrochemical supercapacitors. Nat Nanotechnol 6:232–236
6. Xiang L, Dong YD, Hu Fang WX, Umar A (2018) Co_3O_4 nanowire@NiO nanosheet arrays for high performance asymmetric supercapacitors. Dalton T 47:5697–5694
7. Zhu SJ, Li L, Liu JB, Wang HT, Wang T, Zhang YX, Zhang LL, Ruoff RS, Dong F (2018) Structural directed growth of ultrathin parallel birnessite on #-MnO_2 for high-performance asymmetric supercapacitors. ACS Nano 12: 1033–1042
8. Ghosh K, Yue CY (2018) Development of 3D MoO_3/graphene aerogel and sandwich-type polyaniline decorated porous MnO_2graphene hybrid film based high performance all-solid-state asymmetric supercapacitors. Electrochim Acta 276:47–63
9. Sun X, Li Q, Mao YB (2017) Understanding the influence of polypyrrole coating over V_2O_5 nanofibers on electrochemical properties. Electrochim Acta 2015:563–573
10. Xie MJ, Xu ZC, Duan SY, Tian ZF, Yu Z, Kun X, Lin Ming GXF, Ding WP (2017) Facile growth of homogeneous $Ni(OH)_2$ coating on carbon nanosheets for high-performance asymmetric supercapacitor applications. Nano Res 11: 216–214
11. Wang Y, Zhang XF, Li X, Li XJ, Zhao Y, Wei H, Liu YG, Jiang P, Liang MH (2017) Highly dispersed ultrasmall $Ni(OH)_2$ aggregated particles on a conductive support as a supercapacitor electrode with superior performance. J Colloid Interface Sci 490:252–258
12. Yuan SX, Lu CX, Li Y, Wang XM (2017) Two-step deposition/reduction synthesis of porous lamellar β-$Ni(OH)_2$/reduced graphene oxide composites with large capacitance for supercapacitors. ChemElectroChem 4:2826–2934
13. Armand M, Tarascon JM (2008) Building better batteries. Nature 45(1):652–657
14. Li YH, Zhang SY, Yu QM (2013) Hierarchical porous materials for supercapacitors. Adv Mater Research 750-75:2894-2898
15. Wei JL, Li XR, Xue HG, Shao JY, Zhu RM, Pang H (2018) Hollow structural transition metal oxide for advanced supercapacitors. Adv Mater Interfaces 5: 1701509
16. Yu L, Hu H, Wu HB, Lou XW (2017) Complex hollow nanostructures: synthesis and energy-related applications. Adv Mater 29:1604563
17. Zhou S, Zhao M, Yang TH, Xia YN (2019) Decahedral nanocrystals of noble metals: synthesis, characterization, and applications. Mater Today 22:108–131
18. Hood ZD, Kubelick KP, Gilroy KD, Vanderlaan D, Yang X, Yang MX, Chi MF, Emelianov SY, Xia YN (2019) Photothermal transformation of Au-Ag nanocages under pulsed laser irradiation. Nanoscale 11:3013–3020
19. Zhao C, Huang BY, Fu WB, Chen JY, Zhou JY, Xie E (2015) Fabrication of porous nanosheet-based Co_3O_4 hollow nanocubes for electrochemical capacitors with high rate capability. Electrochim Acta 178:555–563
20. Huang M, Zhao XL, Li F, Li W, Zhang B, Zhang YX (2015) Synthesis of Co_3O_4/SnO_2@MnO_2 core–shell nanostructures for high-performance supercapacitors. J Mater Chem A 3:12852–12857
21. Tian LL, Zhong XH, Hu WP, Liu BT, Li YF (2014) Fabrication of cubic PtCu nanocages and their enhanced electrocatalytic activity towards hydrogen peroxide. Nanoscale Research Letters 9:68–73
22. Xia KD, Yang C, Chen YL, Tian LL, Su YY, Wang JB, Li L (2016) In situ fabrication of $Ni(OH)_2$ flakes on Ni foam through electrochemical corrosion as high sensitive and stable binder-free electrode for glucose sensing. Sens Actuators B Chem 240:979–987
23. Lu P, Liu QB, Xiong YZ, Wang Q, Lei YT, Lu SJ, Lu LW, Yao L (2015) Nanosheets-assembled hierarchical microstructured $Ni(OH)_2$ hollow spheres for highly sensitive enzyme-free glucose sensors. Electrochim Acta 168:148–156
24. Lu P, Lei YT, Lu SJ, Wang Q, Liu QB (2015) Three-dimensional roselike α-$Ni(OH)_2$ assembled from nanosheet building blocks for non-enzymatic glucose detection. Anal Chim 880:42–51
25. Biesinger MC, Payne BP, Lau LWM, Gerson A, Smart SCR (2010) X-ray photoelectron spectroscopic chemical state quantification of mixed nickel metaloxide and hydroxide systems. Surf Interface Anal 41:324–332
26. Li KZ, Li SK, Huang FZ, Lu XY, Wang L, Chen H, Zhang H (2018) Hierarchical core-shell structures of P-$Ni(OH)_2$ rods@MnO_2 nanosheets as high performance cathode material for asymmetric supercapacitors. Nanoscale 10:2524–2532
27. Tian LL, He GG, Cai YH, Wu SP, Su YY, Yan HQ, Yang C, Chen YL, Li L (2017) Co_3O_4 based nonenzymatic glucose sensor with high sensitivity and reliable stability derived from hollow hierarchical architecture. Nanotechnology 29:075502
28. Yan J, Fan ZJ, Sun W, Ning GQ, Wei T, Zhang Q, Zhang RF, Zhi LJ, Wei F (2012) Advanced asymmetric supercapacitors based on $Ni(OH)_2$/graphene and porous graphene electrodes with high energy density. Adv Funct Mater 22:2632–2641
29. Tang Z, Tang CH, Gong H (2012) A high energy density asymmetric supercapacitor from nano-architectured $Ni(OH)_2$/carbon nanotube electrodes. Adv Funct Mater 22:1272–1278
30. Chen J, Wu XF, Selloni A (2011) Electronic structure and bonding properties of cobalt oxide in the spinel structure. Phy Rev B 83:245204
31. Zhang LL, Li HH, Fan CY, Zhang JP (2015) Vertical and cross-linked $Ni(OH)_2$ network on cellulose-fiber covered with graphene as binder-free electrodes for advanced asymmetric supercapacitor. J Mater Chem A 3:19077–19084
32. Tang YF, Liu YY, Yu SX, Gao FM (2015) Template-free hydrothermal synthesis of nickel cobalt hydroxide nanoflowers with high performance for asymmetric supercapacitor. Electrochim Acta 161:279–289

Publisher's Note

Springer Nature remains neutral with regard to jurisdictional claims in published maps and institutional affiliations.

Submit your manuscript to a SpringerOpen journal and benefit from:

- ► Convenient online submission
- ► Rigorous peer review
- ► Open access: articles freely available online
- ► High visibility within the field
- ► Retaining the copyright to your article

Submit your next manuscript at ► springeropen.com